



Full length article

Microscale compressive behavior of hydrated lamellar bone at high strain rates



Cinzia Peruzzi^{a,*}, Rajaprakash Ramachandramoorthy^{a,1}, Alexander Groetsch^a,
Daniele Casari^{a,2}, Philippe Grönquist^{b,c,3}, Markus Rüggeberg^{b,c,4}, Johann Michler^a,
Jakob Schwiedrzik^{a,*}

^a Empa, Swiss Federal Laboratories for Materials Science and Technology, Laboratory for Mechanics of Materials and Nanostructures, Thun, Switzerland

^b Empa, Swiss Federal Laboratories for Materials Science and Technology, Laboratory for Cellulose and Wood Materials, Duebendorf, Switzerland

^c Institute for Building Materials, ETH Zurich, Switzerland

ARTICLE INFO

Article history:

Received 10 March 2021

Revised 30 June 2021

Accepted 2 July 2021

Available online 7 July 2021

Keywords:

Bone

Micropillar compression

High strain rate

Strain rate sensitivity

Deformation and failure mechanisms

ABSTRACT

The increased risk of fracture in the elderly associated with metabolic conditions like osteoporosis poses a significant strain on health care systems worldwide. Due to bone's hierarchical nature, it is necessary to study its mechanical properties and failure mechanisms at several length scales. We conducted micropillar compression experiments on ovine cortical bone to assess the anisotropic mechanical response at the lamellar scale over a wide range of strain rates (10^{-4} to $8 \cdot 10^2 \text{ s}^{-1}$). At the microscale, lamellar bone exhibits a strain rate sensitivity similar to what is reported at the macroscale suggesting that it is an intrinsic property of the extracellular matrix. Significant shear band thickening was observed at high strain rates by HRSEM and STEM imaging. This is likely caused by the material's inability to accommodate the imposed deformation by propagation of thin kink bands and shear cracks at high strain rates, leading to shear band thickening and nucleation. The post-yield behavior is strain rate and direction dependent: hardening was observed for transverse oriented micropillars and hardening modulus increases with strain rate by a factor of almost 2, while axially oriented micropillars showed strain softening and an increase of the softening peak width and work to ultimate stress as a function of strain rate. This suggests that for compression at the micrometer scale, energy absorption in bone increases with strain rate. This study highlights the importance of investigating bone strength and post-yield behavior at lower length scales, under hydrated conditions and at clinically relevant strain rates.

Statement of significance

We performed micropillar compression experiments of ovine cortical bone at two different orientations and over seven orders of magnitude of strain rate. Experiments were performed under humid condition to mimic the natural conditions of bone in a human body using a newly developed micro-indenter setup. The strain rate sensitivity was found to be of a similar magnitude to what has been reported for higher length scales, suggesting that the strain rate sensitivity is an intrinsic property of the bone extracellular

* Corresponding authors at: Empa, Swiss Federal Laboratories for Materials Science and Technology, Laboratory for Mechanics of Materials and Nanostructures, Feuerwerkstrasse 39, 3602 Thun, Switzerland.

E-mail addresses: cinzia.peruzzi@empa.ch (C. Peruzzi), r.ram@mpie.de (R. Ramachandramoorthy), alexander.groetsch@empa.ch (A. Groetsch), daniele.casari@artorg.unibe.ch (D. Casari), groenquist@ibk.baug.ethz.ch (P. Grönquist), markus.rueggeberg@ihd-dresden.de (M. Rüggeberg), johann.michler@empa.ch (J. Michler), jakob.schwiedrzik@empa.ch (J. Schwiedrzik).

¹ Current address: Max-Planck-Institut für Eisenforschung GmbH, Düsseldorf, Germany.

² Current address: ARTORG Center for Biomedical Engineering Research, University of Bern, Bern, Switzerland.

³ Current address: Institute of Structural Engineering, ETH Zurich, Switzerland.

⁴ Current address: Institut für Holztechnologie, Dresden, Germany.

matrix. In addition, localized shear deformation in thick bands was observed for the first time at high strain rates, highlighting the importance of investigating bone under conditions representative of an accident or fall at several length scales.

© 2021 The Author(s). Published by Elsevier Ltd on behalf of Acta Materialia Inc.
This is an open access article under the CC BY-NC-ND license
(<http://creativecommons.org/licenses/by-nc-nd/4.0/>)

1. Introduction

Osteoporosis is the most common metabolic bone disease: Approximately one out of three women and one out of five men over the age of 50 suffer an osteoporotic fracture during their lifetime [1]. With the population aging, this number is even expected to increase [2]. This affects not only the quality of life of the individual patient but also presents a severe socioeconomic burden [2]. To predict the risk of fracture more reliably, it is necessary to gain a better understanding of the deformation and failure mechanisms acting at different length scales through multiscale experimentation and modeling efforts [3,4] in both healthy and diseased state. The most frequent traumatic osteoporotic fractures occur at the wrist and hip [5]. During falls, bone experiences strain rates up to 25 s^{-1} [6]. The strain rates imposed during impacts, accidents, or blast injuries are even higher. Therefore, it is essential to investigate how bone responds to such conditions. However, the micromechanical behavior of bone at high strain rates, especially under humid conditions remains unknown today.

Cortical bone is a hierarchically organized nanocomposite, featuring stiff mineral platelets distributed within a ductile organic phase [7,8]. Its main constituents are hydroxyapatite nanocrystals, collagen and non-collagenous proteins, and water [9,10]. Bone mineral is a less crystalline form of hydroxyapatite that can accommodate ion substitutions such as B-type carbonate [11]. The non-collagenous proteins comprise less than 10% of the organic content [12]. At the microscale, these constituents form mineralized collagen fibrils (MCFs). A fibril consists of staggered collagen molecules with hydroxyapatite mineral platelets arranged in the molecules' gap regions along the fibril's long axis. MCFs are embedded in an extrafibrillar matrix (EFM) that consists of water, mineral and non-collagenous proteins. Bundles of MCFs combine into lamellae, 4–7 μm thick layers that are wrapped concentrically around central blood vessels. Within one lamella the MCFs are uniformly oriented, however, their orientation varies in a rotated plywood pattern [13,14]. Multiple layers of lamellae wrapped around central blood vessels form the so called osteons (diameter 200 μm) that are surrounded by cement interfaces [15]. These structures occupy the majority of cortical bone and are the result of a continuous remodeling process in bone, counteracting the formation of fatigue cracks during every day loading [15]. Bone also features a multiscale porosity: at the microscale, osteocytes occupy the lacuna-canalicular network (LCN) [16,17], whereas at the osteonal level, blood vessels (Haversian and Volkmann canals) permeate bone [18,19]. Cortical bone's anisotropy in material properties such as strength or post-yield behavior is also dependent on the length scale: at the meso- and macroscale, it originates from the osteonal structure, whereas at the microscale, the most influential factor is the local orientation of the MCFs [20]. Therefore, experiments probing different orientations are needed to investigate structure-property relations [9,21]. The present study focuses on the length scale of single bone lamellae allowing to investigate the mineral-collagen nanocomposite properties and the orientation-dependent responses of small, relatively homogeneous volumes (containing MCFs embedded in EFM) as a function of fibril angle.

Common mechanical experiments on the whole bone scale include compressive [22], bending [23], as well as torsion and impact tests [24]. Advantages of testing whole bone samples are that the mechanical environment within the human body can be approximated by applying appropriate boundary conditions. However, it is difficult to identify the influence of the structure or the composition of the material on the measured outcome due to the high level of heterogeneity and potential cross-talk between structural and material effects [25]. Millimeter to centimeter sized samples with a regular shape are usually fabricated for probing material properties on the tissue level (mesoscale). However, at this scale material inhomogeneities, such as Haversian or Volkmann canals, cement interfaces, preexisting microcracks, and heterogeneous mineralization still complicate the interpretation of the test results [25]. Macroscopic volumes in bone inevitably include more material inhomogeneities and defects that can act as local stress concentrators than microscopic bone samples consisting of isolated bone lamellae. Micrometer sized specimens therefore allow assessing the properties of the basic mineral-collagen nanocomposite in relatively homogeneous volumes. It should be noted that while large defects, interfaces, and pores are avoided, smaller scale material inhomogeneities, such as interlamellar interfaces and canaliculi are still present in microscale samples [21]. The majority of the previous micromechanical experiments on bone were carried out at quasi-static strain rates ($\sim 10^{-4} \text{ s}^{-1}$) due to the significant complexities involved in high strain rate testing at these small scales [21–26]. Previous rate-dependent nanoindentation experiments in bone revealed a similar strain rate dependency of the elastic properties to the strain rate dependency of the yield properties of macroscale experiments [27,28]. While nanoindentation is the most common technique used to extrapolate the elastic modulus and hardness [29], the complex and multiaxial stress state under the indenter tip make the interpretation in terms of post-yield properties highly challenging. Micropillar compression has been identified as an alternative method and has been successfully applied at the bone lamella and mineralized collagen fiber level [21,30–34]. Contrary to nanoindentation, micropillar compression results in a largely uniaxial stress state in the specimen, leading to a straightforward analysis in terms of stress-strain behavior. Thus, it renders the determination of the strain rate dependency of the yield properties more straightforward. Previous micropillar compression experiments on dry ovine bone with a diameter of approximately 5 μm showed an increased strength compared to dry macroscale specimens by a factor of 2.4 and an absence of damage at a strain rate of $\sim 5 \cdot 10^{-4} \text{ s}^{-1}$ [32]. Tertuliano et al. found a failure mode transition from ductile to brittle as the size of dry bone pillars decreased from the micrometer to hundreds of nanometers at a strain rate of 10^{-3} s^{-1} [33]. When comparing the existing literature, the compressive yield and strength properties at the length scale of a single lamella fall into a relatively narrow band of 60 MPa irrespective of species. On the other hand, the yield/ultimate stress of rehydrated bone micropillars were found to decrease by approximately 60 % compared to dry samples [21], underlining the importance of testing under near-physiological conditions.

To the best of our knowledge, no high strain rate experiments have been performed so far on bone on the microscale. This is a

significant knowledge gap, as it can help to identify the hierarchical scales and phases from which bone's strain rate dependence of mechanical properties and failure mechanisms originates. It further allows us to mimic the conditions under which bones normally break, e.g. during a fall or impact. To achieve these goals, we developed a micromechanical testing setup that allows us to perform displacement-controlled high strain rate experiments inside a humidity chamber. Using this setup, we conducted micropillar compression with two distinct fiber orientations at strain rates spanning six orders of magnitude from 10^{-4} s^{-1} to $8 \cdot 10^2 \text{ s}^{-1}$.

2. Methods

2.1. FIB - Micropillar fabrication

A tibia of a two year old sheep was obtained from a local abattoir. Two samples from the same quadrant of the diaphysis of the tibia were used, one cut perpendicular to the long axis of the diaphysis (axial specimen), and one cut in radial direction (transverse specimen). Both the samples were cut within regions containing a significant amount of osteonal bone. The samples were then directly glued to standard scanning electron microscopy (SEM) stubs using a surface insensitive adhesive (ergo 5011, Kisling, Switzerland) and ultramilled with diamond blades (Polycult E, Reichert-Jung, Germany) for the surface to be sufficiently flat and parallel for micromechanical experiments. Micropillars were then fabricated by eroding material using a focused ion beam (FIB) (Tesla, Czech Republic). To minimize drift during fabrication, a 10 nm layer of gold was sputtered on the samples (Leica EM ACE600, Germany). A three-step procedure was used at a beam energy of 30 kV. A coarse milling step at a current of 8 nA cut an annular trench with an outer diameter of 50 μm and an inner diameter of 16 μm . A second step at 1.5 nA brought the inner diameter of the annulus to 8 μm . A polishing step at 1 nA then cut the micropillars to their final dimensions of approximately 5 μm . A total of 93 micropillars were produced (46 in axial and 47 in transverse orientation). In order to probe individual lamellae, micropillars were produced with a diameter of $5.52 \pm 0.14 \text{ }\mu\text{m}$ and a height of $10.35 \pm 0.68 \text{ }\mu\text{m}$ (aspect ratio of around 2). The micropillars show a taper of 2.4° . The dimensions of the micropillars were quantified using a high-resolution scanning electron microscope (HRSEM, Hitachi S-4800, Japan) operated at 1.5 kV and 10 pA at a tilt angle of 55° with no additional coating of the sample after the FIB milling.

2.2. High strain rate indenter with humidity setup

A new *ex situ* indentation setup was developed to perform micromechanical experiments under controlled environmental conditions (Fig. 1). The system features a humidity chamber, in which relative humidity (RH) can be controlled between 5–95% using a continuous gas stream from an external humidity generator (SE-TARAM Wetsys, France). The relative humidity and temperature of the gas is measured constantly in the chamber using an external sensor with a precision of $\pm 1.5\%$ RH at ambient temperature (Rotronic Hygroclip HC2-SC05, Switzerland). To ensure the relative humidity is homogeneously distributed within the chamber, it was measured at different locations within the chamber, i.e. above as well as next to the sample. The measured difference is smaller than 1% RH at the different locations, therefore it may be treated as constant within the chamber. The lid on top of the chamber features an opening above the sample to both observe the sample surface when placed under a microscope and to allow the indenter tip to reach the specimen surface. An optical microscope is used to visualize the sample surface and to set the points of interest on the sample. Once the coordinates are saved, a calibrated X and Y

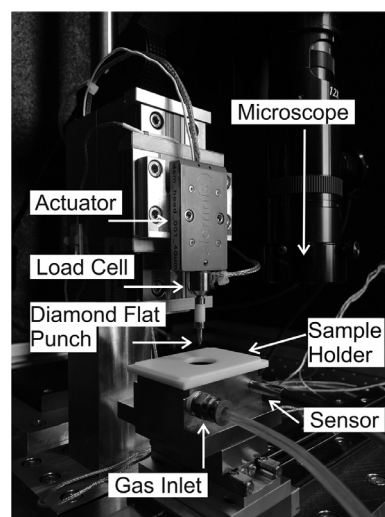


Fig. 1. Ex situ indenter. The load cell and tip are mounted on a vertical linear rail. The sample holder is positioned on an x- and y-stage with micrometer precision and can be moved to the microscope. The sample holder comprises a chamber with two inlets: one for the humid gas and one for the humidity and temperature sensor.

stage is able to translate and position the sample underneath the indenter tip with a precision of $\sim 1 \text{ }\mu\text{m}$.

A high-stiffness load cell (Alemnis AG, Switzerland) is mounted on a vertically installed coarse linear rail positioner to account for different specimen heights. During the tests, displacements are applied using a piezoelectric actuator (Alemnis AG, Switzerland) with a range of 40 μm and a resonance frequency of $\approx 4 \text{ kHz}$. This setup allows for displacement-controlled experiments, which is important to maintain a constant strain rate, especially beyond the materials' yield point. Using the system with the standard load cell (stiffness = $1.667 \cdot 10^6 \text{ N/m}$, resonance frequency $\approx 10 \text{ kHz}$) allows to perform experiments up to a speed of 1 $\mu\text{m/s}$ and a maximum force of 500 mN. At a sampling frequency of 40 Hz, the root mean square (RMS) displacement and load noise are in the order of 0.150 mN and 0.1 nm, respectively, and increase to 0.300 mN and 10 nm for a sampling frequency of 5 kHz.

For high strain rates, the load cell is replaced by a piezoelectric force sensor that has been extensively validated and used in scientific studies on various materials [35–38] (Alemnis AG, Switzerland, stiffness = $2.56 \cdot 10^7 \text{ N/m}$, resonance frequency $\approx 40 \text{ kHz}$). This allows to conduct experiments with an actuation velocity of up to $\sim 10 \text{ mm/s}$. Force and displacement are measured using high speed electronics (Alemnis AG, Switzerland) up to a sampling frequency of 1 MHz, allowing to capture high-resolution force-displacement curves even during high displacement speeds. The RMS displacement noise for a sampling frequency of 1 MHz is below 200 nm and the RMS load noise is $\sim 3 \text{ mN}$. To reduce the influence of oscillations of the system due to these high actuation velocities the displacement is set to the maximum so the indenter travels first through air and is in contact with the sample only once the oscillations died down. For further details, see Supplementary Fig. 8 in the Supplementary Information.

2.3. Sample hydration

Commonly samples are hydrated immersing them in water or a solution. Often, a 0.9% NaCl solution is used, as it is considered isotonic, meaning that the intracellular fluids and the extracellular fluids are in osmotic equilibrium and therefore, cell volume change is prevented [39,40]. However, salt ions are sufficiently small to enter collagen unhindered and do not form osmotic pressure in collagen fibrils, unlike when interacting with a semiper-

meable membrane [41]. In this study we used a new method to keep the sample hydrated by continuously flushing it with water vapor while keeping the relative humidity within the chamber above 90%.

2.4. Dynamic vapor sorption

Dynamic vapor sorption (DVS) is a gravimetric method that measures the change in mass of a sample as a function of relative humidity [42]. The DVS isotherm was determined (DVS Advantage ET85, Surface Measurement Systems Ltd.) for two samples of ovine bone with the dimensions of approximately 3 mm x 3 mm x 1 mm. The samples were dried for 48 hours at 40°C. The temperature was then lowered to 27°C, and the weight of the samples was measured as a function of relative humidity in the chamber. Mass equilibrium at a given humidity step was assumed to be reached when the change in mass was less than 0.0001%/min (Supplementary Information, Supplementary Fig. 3).

2.5. Micropillar compression at humid conditions and high strain rates

Micropillar compression tests were performed at ambient temperature and pressure and the relative humidity was set to over 90% to approximate physiological conditions. The micropillars were compressed using a flat punch diamond tip, i.e., a truncated cone with a diameter of the contact surface of 20 μm . A strain rate range over seven orders of magnitude from 10^{-4} s^{-1} to $8 \cdot 10^2 \text{ s}^{-1}$ was explored using two different force sensors. During the experiments, load and displacement signals were recorded continuously. For slow strain rates (10^{-4} s^{-1} to 10^{-1} s^{-1}), a standard load cell was used in displacement control and the micropillars were compressed to 0.5–1 μm corresponding to 5–10% strain. For high strain rates (1 s^{-1} to $8 \cdot 10^2 \text{ s}^{-1}$) a piezoelectric force sensor was used in open loop. Due to the short times of the high strain rate experiments and the resulting inability to observe them in realtime they were compressed further to 1.5–2 μm corresponding to 15–20% strain. These strains are well beyond the elastic limit of lamellar bone. For both transverse and axial direction samples, at each order of strain rate magnitude, 4–8 micropillars were compressed. Before and after mechanical testing, all micropillars were imaged by HRSEM (HRSEM, Hitachi S-4800, Japan) at a voltage of 1.5 kV and a current of 5 nA to identify the initial shape and deformation induced during the experiment. In the high resolution images cracks are visible on the surface of the micropillars. These cracks as well as their angles were recorded manually for every micropillar. The angles of the cracks were measured with ImageJ (ImageJ 1.53a, National Institutes of Health, USA).

2.6. FIB – cross-section

To understand the deformation mechanisms in more detail, cross-sections of six compressed micropillars showing representative yield properties and deformation patterns in the HRSEM analysis were fabricated at a beam energy of 30 kV (Tescan, Czech Republic). A two-step procedure was used. One third of the micropillars cross-section was polished at 200 pA. For a fine surface finish, the last slice was then milled at 50 pA.

2.7. Scanning transmission electron microscopy (STEM)

Three bone micropillars compressed at 10^2 s^{-1} and $8 \cdot 10^2 \text{ s}^{-1}$ and showing representative yield properties as well as deformation patterns in the HRSEM analysis were chosen for a near atomic resolution STEM investigation, to better analyze the deformation mechanisms at high strain rates. A previously established lift-out

technique was employed to prepare a 200 nm thin lamella from the central section of the deformed pillars [21]. Bright-field STEM images were collected in a HRSEM (HRSEM, Hitachi S-4800, Japan). The microscope was operated using a transmission electron detector, with the electron beam acceleration voltage of 30 kV and current of 10 μA .

2.8. Data analysis

Micropillar compression results in a largely uniaxial stress state. Therefore, the stress-strain data, as well as the yield properties can be extracted from the load displacement data using the known dimensions of the micropillars. These properties were determined for every micropillar using a custom Matlab (R2018a, The MathWorks, USA) code. To reduce noise, the load data was smoothed with a moving average filter with a span of 2% of the length of the data. The load data for the axial micropillars that were compressed with a velocity of 8.5 mm/s had a significantly increased noise level. As such, instead of averaging, it was fitted with a high order polynomial. The fits resulted in a R^2 value between 0.996 and 0.998. Engineering stress was then calculated by dividing the load by the micropillar's top surface area. Engineering strain was defined by dividing the displacement of the flat punch after contact with the micropillar by the initial height of the micropillar. The machine compliance was calibrated using a fused silica sample and the compliance of the base of the micropillar, that is also bone, was accounted for using the modified Sneddon correction [43]. The yield stress was computed as the stress that is needed for an inelastic strain of 0.2%.

In addition, for the axial micropillars, ultimate stress and a plateau stress were calculated. The ultimate stress was defined as the maximum stress in the stress overshoot peak. For the calculation of plateau stress, the stress-strain curve (Fig. 2) was numerically differentiated. Subsequently, the minimum of the differentiated stress curve was determined, which corresponds to the turning point of the slope of the stress-strain curve after the stress overshoot. From this strain to the maximum strain, it was iteratively checked whether the average of 20 data points is smaller than 10% of the maximum of the differentiation. When this condition was reached, it was determined that the slope is sufficiently close to zero for the stress to be defined as plateau stress.

Further, the overshoot curve before the ultimate stress for the axial pillars was checked for a stress equal to the plateau stress. From this stress point to the plateau stress, strain and stress were determined, along with the full width at half maximum, calculated as a quantification of the width of the hardening/softening peak (Fig. 3b). Additionally, the ultimate stress to yield stress and the plateau stress to yield stress ratios were determined. Finally, the work to ultimate stress was defined (Fig. 3c) by integrating the stress curve up to the ultimate stress with the trapezoidal numerical integration function of Matlab (R2018a, The MathWorks, USA).

For the transverse micropillars, the hardening modulus was determined (Fig. 3d). Specifically, it was defined as the slope of the stress between the yield strain plus 0.02 and the maximum strain minus 0.02 was identified using a linear fit. Schematics showing the definition of these parameters are included in the Supplementary Information (Supplementary Figs. 4 and 5).

2.9. Thermal activation analysis

To quantify the strain rate dependency, we calculated the strain rate sensitivity, which is the proportionality factor between the logarithm of the yield stress and the logarithm of the strain rate [44,45]. The formula for the strain rate sensitivity exponent at con-

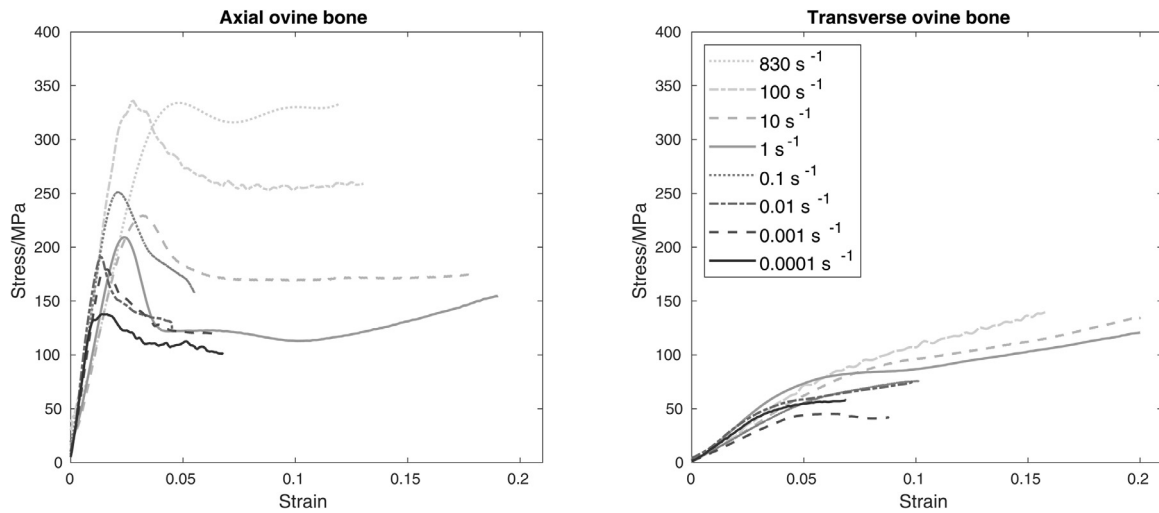


Fig. 2. Representative stress-strain curves for different strain rates for axial (left) and transverse (right) micropillars. The legend applies to both graphs.

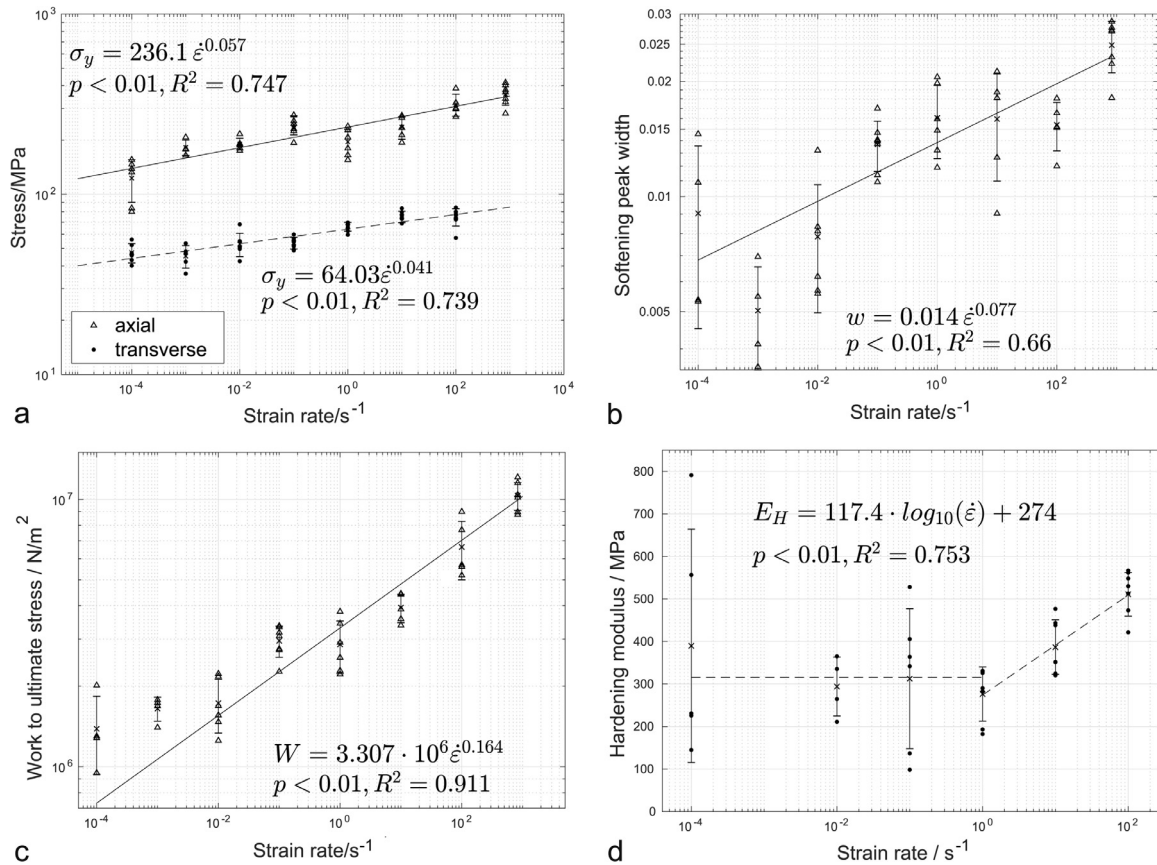


Fig. 3. (a) Yield stress extracted from lamellar bone micropillar tested at different strain rates in the axial and transverse direction. (b) The softening peak width for the axial experiments was quantified by calculating the full width at half maximum of the overshoot in the stress strain data. The data is presented on a log-log scale and a power function was fitted to the data (solid line). The trend is significant ($p < 0.01$). (c) The work to ultimate stress for the axial micropillars increases significantly ($p < 0.01$) with increasing strain rate. (d) Hardening modulus for transverse micropillars.

stant temperature is defined as [45]:

$$m = \left[\frac{d(\ln \sigma)}{d(\ln \dot{\epsilon})} \right]_T \quad (1)$$

with σ as yield stress, $\dot{\epsilon}$ as strain rate and T as temperature.

Furthermore, from the change in yield stress over the strain rate, the activation volume can be calculated. In metals this is a volume usually given in proportion to the Burger's vector and it

is a well-established measure to determine the amount of matter involved in deformation process [46]. In polymers it is associated with the movement of flow units, which are segments of larger molecules [47]. It can be calculated with the following formula [48]:

$$v = \sqrt{3} k_B T \left. \frac{d(\ln \dot{\epsilon})}{d \sigma} \right|_T \quad (2)$$

with k_B is the Boltzmann constant, T the temperature during the experiments, $\dot{\epsilon}$ the strain rate and σ the yield stress. A line was fitted to the natural logarithm of the strain rate as a function of the yield stress. Then the slope of this line was used to determine the activation volume. It should also be noted that the 0.2% offset strain method was used to identify the yield stress, and the apparent strain rate sensitivity and activation volume were calculated based on this yield stress. Therefore, we assume that, at yield, the bone microstructure is approximately constant during the different micropillar tests.

2.10. Statistical analysis

The p-values of the fitted trend lines were computed with the correlation coefficient function of Matlab (R2018a, The MathWorks, USA), with a significance level of $\alpha = 0.01$ and the coefficient of determination R^2 was directly taken from the fitting function.

2.11. Thermal modeling

To assess possible effects of heating during high strain rate deformation, axisymmetric thermal finite element simulations were performed using Comsol (Comsol Multiphysics 5.5, COMSOL Inc., USA). Thermal simulations were performed to evaluate whether dissipative heating during mechanical compression could have a significant effect on the measured micromechanical properties of bone. Three possible cases of heating were considered: heating within a single thin shear band, heating within a single thick shear band, and heating within several shear bands which translates to bulk heating of the micropillar. The micropillar was modeled standing on a bone substrate with 25 μm radius and height. The thermal material properties were taken from the literature [49] with heat capacity at constant pressure $C_p = 1260 \text{ J/kgK}$, density $\rho = 2000 \text{ kg/m}^3$, and thermal conductivity $k = 0.64 \text{ W/mK}$. The boundaries of the simulated substrate to the infinite halfspace below were modeled as constant temperature boundaries, e.g. it was assumed and verified that they are sufficiently far away from the micropillar not to affect the solution. A mesh was generated consisting of 1052 triangular domain elements and 100 boundary elements. The effects of radiative and convective heat loss on the boundaries exposed to air were not considered. For the boundary at the top of the micropillar in contact with the indenter two different cases were modeled: An isolated boundary to model a high interfacial thermal resistance between indenter and micropillar and a constant temperature boundary assuming that the indenter acts as a heat sink and the interfacial thermal resistance is negligible. For the highest experimental strain rates, either volumetric heating of the micropillar through dissipation due to bulk plastic deformation of the whole micropillar or due to plastic dissipation inside a 2.5 μm thick shear band were considered. For the former, the plastic energy was determined by integrating the area under the experimental stress-strain curve, subtracting the elastic contribution, and dividing by experimental duration. This power was introduced into the micropillar as a body heat source. For the latter, the stress-strain behavior was calculated under the assumption that all plastic deformation takes place in a 2.5 μm thick shear band oriented at 45° to the loading axis, and used for the following power calculation analogous to what was described for the bulk heating deformation of the whole. Thermal simulations were run for the full duration of the experiment and the maximum temperature rise in the micropillar was calculated.

3. Results

Representative stress-strain curves for which the yield stress was observed to be closest to the average yield stress of the par-

ticular strain rate, are shown in Fig. 2. The axial micropillars were compressed up to a maximum strain rate of $8 \cdot 10^2 \text{ s}^{-1}$, while the highest strain rate for the transverse micropillars was restricted to 10^2 s^{-1} due to a lower signal to noise ratio of the force measurement, as the transverse micropillars yield at a considerably smaller force. The overall strain rates of the axial micropillars feature a pronounced strain softening behavior in the plastic region, whereas the transverse samples show linear strain hardening.

Based on the extracted yield stresses, the strain rate sensitivity exponent m was calculated to be equal to 0.057 (95% confidence interval 0.047 to 0.068) and 0.041 (95% confidence interval 0.033 to 0.048) for axial and transverse micropillars, respectively. The activation volume of the underlying dominant inelastic deformation mechanism was computed using Eq (2) and was found to be $v = 0.400 \text{ nm}^3$ for the axial and $v = 2.160 \text{ nm}^3$ for the transverse experiments.

The stress-strain curves of the axial specimens showed a pronounced softening peak after yielding. The full width at half maximum of the softening peak was determined as a function of strain rate as shown in Fig. 3b. A power function was fitted to the data highlighting a significant trend ($p < 0.01$, $R^2 = 0.66$).

To quantify the strain rate dependency of the softening behavior observed in axial micropillars, the ultimate stress, work to ultimate stress, as well as the ratios of ultimate stress to yield stress and plateau stress to yield stress were analyzed as a function of strain rate. The ultimate stress increased significantly from $129.3 \pm 29.1 \text{ MPa}$ at a strain rate of 10^{-4} s^{-1} to $381.5 \pm 54.6 \text{ MPa}$ at $8 \cdot 10^2 \text{ s}^{-1}$ ($p < 0.01$, $R^2 = 0.747$). Furthermore, the work to ultimate stress was determined as a surrogate measure for toughness and analyzed as a function of strain rate (Fig. 3c). A significant increase was found by fitting a power function ($p < 0.01$, $R^2 = 0.911$) highlighting a clear trend in the data. For the ultimate stress to yield stress ratio, we found a significant correlation to the strain rate ($p < 0.01$). However, R^2 was relatively low (0.38) and the slope corresponds to an increase of less than 6% over seven orders of magnitude in strain rate. For the ratio of plateau stress to yield stress, no significant correlation was found ($p > 0.01$). The scatter plots of the ultimate stress to yield stress ratio as well as the ratio of the plateau stress to yield stress are included in the Supplementary Information (Supplementary Figs. 6 and 7).

For the transverse micropillars, the hardening modulus in the post-yield region was calculated from the stress-strain data (Fig. 3d). The curves with a strain rate of 10^{-3} s^{-1} did not show strain hardening and were therefore excluded from this analysis. The hardening modulus was found to be constant for low strain rates using linear regression analysis ($p > 0.01$). However, a significant increase in the hardening modulus was found for strain rates of 10^0 s^{-1} and above ($p < 0.01$, $R^2 = 0.753$). In this range, the hardening modulus increases by almost a factor of 2 over two orders of magnitude in strain rate.

Post-test SEM images reveal that cracks have formed during the compression tests. Axial micropillars show axial splitting corresponding to distinct, almost vertical cracks ($86.3 \pm 15.8^\circ$, number of cracks observed on all axial pillars = 100). This is the case for all the axial micropillars over all tested strain rates (Fig. 4). Transverse micropillars are laced with a web of fine cracks. These cracks are oriented at shallower angles ($31.7 \pm 11.2^\circ$, number of cracks observed on all transverse pillars = 168) and often parallel to each other. For strain rates of 10^0 s^{-1} and higher, it becomes increasingly difficult to spot distinguished cracks, because their number increases and their size decreases (for more information see Supplementary Information).

To further investigate the dominant failure mechanisms, FIB cross-sections of six micropillars were imaged using a high-resolution SEM (Fig. 5). To minimize bias in the selection of micropillars, we selected the micropillars with the yield stress

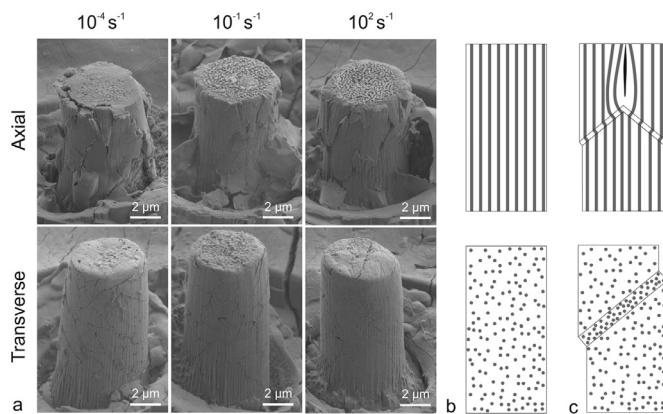


Fig. 4. (a) HRSEM images of axial (top) and transverse (bottom) micropillars after compression for strain rates of 10^{-4} s^{-1} (left), 10^{-1} s^{-1} (middle) and 10^2 s^{-1} (right). The shown micropillars are the ones corresponding to the representative curves from Fig. 2. The maximum strain for the axial micropillars is equal to 0.068 (left), 0.056 (middle) and 0.148 (right) and for the transverse micropillars 0.069 (left), 0.102 (middle) and 0.173 (right). (b) schematic of undeformed micropillars. Grey lines and dots represent the fibrils that are parallel or perpendicular to the long axis for the axial and the transverse micropillars respectively. (c) schematic of deformed micropillars

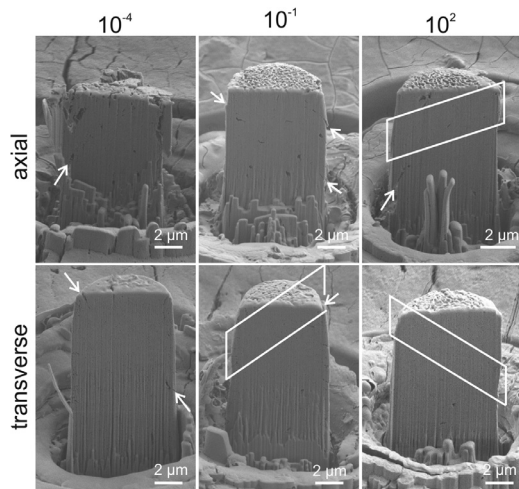


Fig. 5. FIB cross-section of axial (top) and transverse (bottom) micropillars after compression for the strain rates of 10^{-4} s^{-1} (left), 10^{-1} s^{-1} (middle) and 10^2 s^{-1} (right). The maximum strain for the axial micropillars is equal to 0.075 (left), 0.063 (middle) and 0.165 (right) and for the transverse micropillars 0.065 (left), 0.098 (middle) and 0.181 (right). The white arrows indicate cracks, the parallelograms deformation zones. The vertical lines seen in all the pillars are a FIB artifact known as curtaining or waterfall effect and it is often seen when milling porous materials or composites of hard and soft materials.

closest to the mean yield stress for the given strain rate. Furthermore, it was checked that the deformation behavior shown by these micropillars was representative of their respective cohort based on the post-test HRSEM images. For axial micropillars tested at 10^{-4} s^{-1} and 10^{-1} s^{-1} as well as the transverse micropillar for the quasi-static strain rate (10^{-4} s^{-1}), shear cracks are clearly visible (Fig. 5, white arrows). For the transverse micropillars compressed at higher strain rates (10^{-1} s^{-1} and 10^2 s^{-1}), no such crack is visible, however, the micropillar bulges (Fig. 5, parallelograms) suggesting deformation within a finite shear zone. The axial micropillar compressed at 10^2 s^{-1} shows both deformation mechanisms. The thickness of the shear bands was found to be 1–2.5 μm (For further details see Supplementary Fig. 1 in the Supplementary Information).

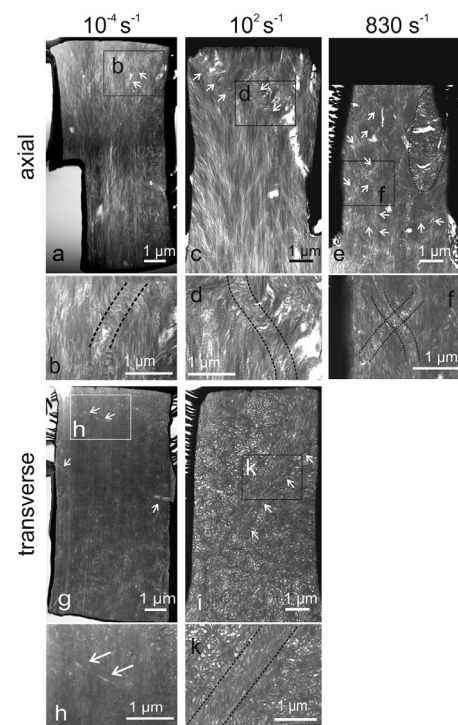


Fig. 6. STEM images of transverse (g and i) and axial (a, c and e) micropillars after compression for strain rates of 10^{-4} s^{-1} (a and g) of 10^2 s^{-1} (c and i) and $8 \cdot 10^2 \text{ s}^{-1}$ (e). Below the micropillars the according magnifications are presented. The maximum strain for the micropillars is equal to 0.173 (i), 0.148 (c) and 0.158 (e). The white arrows in (g) indicate cracks in the other images they indicate shear bands. The region within the dotted line for the axially compressed micropillar at $8 \cdot 10^2 \text{ s}^{-1}$ (e) is considered to be a region of the interlamellar interface. The micropillars shown in images (c, e and i) are the ones corresponding to the representative curves from Fig. 2. The images of the micropillars compressed at quasi-static strain rate (a and g) were collected in an earlier study [21].

STEM images were collected for three micropillars showing representative mechanical response (two axial and one transverse) compressed for the strain rates of 10^2 s^{-1} (axial and transverse) and $8 \cdot 10^2 \text{ s}^{-1}$ (axial) (Fig. 6). Mineralized collagen fibrils oriented perpendicular to the image plane appear as white spots (Fig. 6g and i) [50]. In the shear band (Fig. 6i and k) these perpendicular collagen fibrils cannot be observed due to the high shear deformation (thickness 650nm). The axial micropillars show fibrils that are highly aligned along the pillar long axis. The axial micropillar compressed at a strain rate of 10^2 s^{-1} shows two distinct shear bands (white arrows in Fig. 6c, thickness 370 nm). The axial micropillar compressed at a strain rate of $8 \cdot 10^2 \text{ s}^{-1}$ shows a high number of thin shear bands (thickness 290 nm) in a cross-hatched pattern within the whole micropillar volume (Fig. 6e).

Furthermore, STEM images of ovine bone micropillars compressed at a quasi-static strain rate (10^{-4} s^{-1}) collected in an earlier study [21] are shown in Fig. 6. Three cracks are visible in the transverse micropillar (indicated with white arrows Fig. 6g). In the axial micropillar, a thin kink band with a thickness of $124 \pm 13 \text{ nm}$ is visible [21].

When considering a localized heat source based on plastic dissipation in a shear band of 2.5 μm thickness for a strain rate of 10^2 s^{-1} , the maximum temperature reached in the micropillars was calculated to be 312 K / 309 K in axial and 300 K / 299 K in transverse direction depending on the boundary condition on the top of the pillar (isolated boundary/constant temperature boundary). If the shear band thickness is reduced to 125 nm in the simulation based on an earlier quasi-static study [21], the maximum temperature is rising to 315 K / 312 K. When considering bulk

heating due to plastic deformation within the whole pillar volume, the maximum temperature reached within the tested volume was computed as 310 K / 307 K in axial and 299 K / 298 K in transverse direction, respectively. Simulations for the axial micropillar tested at $8 \cdot 10^{-2} \text{ s}^{-1}$ showed that the boundary conditions in this case have only a minor influence and that the maximum temperature remained approximately constant compared to 10^2 s^{-1} at 312.5 K.

4. Discussion

4.1. Micropillar compression

The yield stress of the micropillars in axial direction interpolated for the strain rate of $5 \cdot 10^{-4} \text{ s}^{-1}$ (153.1 MPa) agrees with earlier findings on hydrated ovine bone reported by Schwiedrzik et al. [21] ($171 \pm 22 \text{ MPa}$). The yield stress for the transverse micropillars was found to be lower in this study ($47.4 \pm 5.8 \text{ MPa}$ vs $126 \pm 25 \text{ MPa}$ [21]). This is likely caused by swelling artifacts that are more pronounced in transverse micropillars than in the axial ones due to the fibril alignment parallel to the surface [51]. For dry conditions, a yield stress of $327 \pm 20 \text{ MPa}$ on micropillars fabricated on trabecular human bone with a diameter of $3 \mu\text{m}$ at a strain rate of $1 \cdot 10^{-3} \text{ s}^{-1}$ was found [33]. Also under dry conditions Indermaur et al. [52] found a yield stress of $350 \pm 97 \text{ MPa}$ when compressing micropillars of healthy human bone as well as samples with osteogenesis imperfecta with a diameter of $5 \mu\text{m}$ and at a strain rate of $5 \cdot 10^{-4} \text{ s}^{-1}$. When considering the reduction of yield stress of 60% due to hydration of the tissue reported earlier [21], these measurements fall within the same range measured for ovine bone in this work. This highlights the relatively small variation found in compressive yield properties of bone measured in different species.

A clear anisotropy was found in this study with the yield stress of the transverse micropillars being consistently smaller by a factor of 2.5–4.5 compared to the axial direction. This is consistent with literature at several length scales measured by nanoindentation [53], micropillar compression [21], or macroscopic compression experiments [54].

Axial micropillars show a strain softening post-yield behavior. Combined with the HRSEM images, where distinct vertical cracks, as well as local shearing are visible, this suggests that the matrix starts flowing under load leading to a local shear instability. This leads to kink band formation, described also in micropillar studies performed at quasi-static strain rates [21,31] and observed here in the STEM images (Fig. 6). Pimenta et al. [65] observed a similar behavior in fiber reinforced composites and found that when such composites were compressed along the fiber axis, the matrix material yields in shear and, as a consequence, kink bands are formed. When zones of localized shear deformation meet, a wedge of material is formed that splits the micropillar vertically, which explains the observed axial splitting failure.

The transverse specimens showed strain hardening at almost all strain rates which is in line with earlier microcompression studies at quasi-static strain rates [21], as well as compressive experiments of macroscopic antler specimens, a similar mineralized tissue [55]. Wood, in comparison to bone, is mainly based on polymers; however, on the microscale it is as bone a nanofiber reinforced composite and shows a similar orientation-dependent post-yield behavior over varying strain rates [56]. In contrast to the axial case, where the fibers are loaded like springs before plastic deformation starts, in the transverse samples we hypothesize that under loading the fiber spacing decreases until a threshold is reached and plastic deformation is initiated similarly to the deformation mechanism reported for wood [56]. This is in agreement with nanoindentation experiments on bovine bone conducted in transverse direction [57] showing a lack of pile-up surrounding the imprint due

to the compaction of the tissue. A similar post-yield anisotropy was found on micropillar compression of hydrated bovine bone samples with the same nominal dimensions as the micropillars in the current study [51]. Where a method was developed based on polarized Raman spectroscopy that allows identifying the 3D collagen orientation locally. Softening in the post-yield regime was observed for micropillars with a collagen fibril angle of not more than 30° from the micropillar axis (axial samples). Micropillars with collagen fibrils deviating by $60\text{--}90^\circ$ from the micropillar axis (transverse samples) were found to consistently show strain hardening, which is in line with the findings of this study.

The width of the softening peak was found to increase significantly with strain rate. Together with the increase of the work to ultimate stress, this suggests that more energy is absorbed at higher strain rates. The total energy absorbed until failure could not be used to define toughness, as the micropillars did not fail even at high strains and therefore no failure strain could be determined. As a surrogate measure of toughness, the work to ultimate stress was determined for the axial micropillars instead. It increases over an order of magnitude as the strain rate was increased from 10^{-4} s^{-1} to $8 \cdot 10^{-2} \text{ s}^{-1}$. According to finite elements simulations [61], bone's toughness arises from the staggered fibrillar alignment in combination with a cohesive interface between fibrils. Interfacial failure mechanisms, such as the breaking of sacrificial bonds within the interfibrillar matrix, also play a crucial role in the toughness of bone [58,59]. It was not possible to determine a similar surrogate measure of toughness for the transverse micropillars based on the mechanical data, as they did not fail even at high strains and consistently showed a hardening post-yield behavior.

However, for tensile experiments at the micrometer scale a brittle failure behavior was observed [60]. Therefore, more tensile experiments at the microscale are needed to better understand this tension-compression strength asymmetry.

4.2. Strain rate sensitivity

Strain rate sensitivity was slightly more pronounced for the axial micropillars than for the transverse micropillars ($m = 0.057$ in axial, $m = 0.041$ in transverse). Our results are in good agreement with the strain rate sensitivity of macroscale human and bovine bone ($m = 0.06$) deformed at similar strain rates ($10^{-4} - 10^2 \text{ s}^{-1}$) [44]. Previous poro-elastic analysis of indentation on hydrated bone at the microscale showed a significant change in time-dependent mechanical properties [61]. Size effects in bone are typically attributed to the interfaces between lamellae and surrounding osteons [62]. In the current study, the strain rate sensitivity was found to be similar on the micro- and macroscale and agrees with data from different types of mineralized tissues with varying mineralization [44]. The mineral/matrix ratios ($\nu_2\text{PO}_4^{3-}/\text{Amide III}$) of the samples used in this study was measured using Raman spectroscopy in an earlier study [60] and found to be 0.63 ± 0.05 and 0.76 ± 0.08 for the axial and the transverse sample, respectively. While the absolute strength values differ, the strain rate sensitivity remained comparable within a small band of 0.03 to 0.1 [27,28,44]. This suggests that the strain rate sensitivity of the yield stress in bone is an intrinsic property of the bone extracellular matrix and does not significantly depend on the degree of mineralization. The lack of mesoscale internal interfaces in the micropillars like interlamellar and cement interfaces, or large pores such as Haversian canals, which have been suggested to play a major role in the dynamic behavior of bone [63] further supports the idea that the strain rate sensitivity is an intrinsic property of the bone extracellular matrix, as we could show that it exists already at the level of the bone lamella.

4.3. Thermal activation analysis

The activation volume calculated using Eq (2) is a measure of how many atoms are involved in the inelastic process [64] and is often used in materials science to identify the dominating nanoscale deformation mechanisms. In this work, it was calculated to be 0.4 nm³ and 2.16 nm³ for the axial and transverse cases respectively. This is in the same order of magnitude as the reported value for bovine bone (0.6 nm³) [26]. It has been suggested that the bonds breaking during inelastic deformation are charge interactions between molecules in the extrafibrillar matrix or glue layer between the mineralized collagen fibrils [26]. This is in line with our interpretation that yielding starts in the extrafibrillar matrix, which leads to kink band formation through buckling of MCFs [21,65] in axial micropillars and shear band formation between MCF in transverse micropillars. This can be seen in STEM images of micropillars compressed at quasi-static strain rates that originate from a previous study [21] as well as for high strain rate compression (Fig. 6). The activation volume for glassy polymers is reported to be within 1.3 – 17 nm³ and is related to localized plastic deformation bands that propagate through the sample [47]. The difference in the activation volume for axial and transverse orientation is not necessarily an indication of a change in deformation mechanism, as both values are at the lower end of the activation volume spectrum for polymers.

4.4. Deformation mechanisms

To investigate the deformation mechanisms in more detail, the stress strain data with and HRSEM images from all the micropillars before and after compression were considered. Then, a subset of representative micropillars was selected based on their yield properties and observed deformation mechanisms to further analyze by means of FIB cross sectioning and STEM imaging. The FIB cross-sections of the axial micropillars suggest that the majority of the plastic deformation is localized within shear zones, which was also shown by STEM imaging [21] and is in agreement with the compressive damage zone model [66]. In this model, longitudinal microcracks develop before ultimate stress is reached. These microcracks absorb energy and finally coalesce leading ultimately to failure. The interaction of fibers with microcracks consumes large amounts of energy. At lower strain rates, the microcracks have time to extend and less fibers take part in the interaction with the crack. This is also observed in the STEM images (Fig. 6) where for high strain rates the number and thickness of sheared zones is increased compared to quasi-static strain rates [21]. Interestingly, similar effects have been reported also for carbon fiber reinforced composites, where the number of microcracks nucleating increases with strain rate resulting in more fragmented specimens [67]. Therefore, despite the differences between these fiber reinforced composite materials representing a composite of hard reinforcements in a soft matrix, which is not necessarily the case for bone tissue, similar failure mechanisms can be observed at high strain rates. For the transverse experiments, strain hardening was observed for a vast majority of the curves. The hardening modulus was found to be constant in the strain rate range 10⁻⁴ – 10⁻¹ s⁻¹ and increases significantly for higher strain rates. This increase in strain hardening is a highly viscous process and is in agreement with models of strain hardening in glassy polymers [68,69]. It has been previously suggested that bone densifies when loaded normal to MCF direction [57]. As the mineral particles are displaced within the organic matrix during densification, it can be argued that at higher strain rates the organic phase does not have sufficient time to rearrange causing the mineral particles to become entangled and blocking their relative movement. This would also explain why, for high strain rates, no distinct micro-

cracks are visible in Fig. 5 and Fig. 6, but a thick shear deformation zone that seems to depend on the applied strain rate can be observed. This is in line with strain hardening in glassy polymers that is related to the required rate of plastic rearrangements for maintaining chain connectivity and the increase in size of the regions that must therefore undergo plastic deformation in response to shear [37,70].

4.5. Thermal Modeling

Thermal modeling allowed us to estimate the effect of deformation induced heating on the measured micromechanical properties of bone at high strain rates. The maximum temperature in the micropillar due to localized plastic deformation within a shear band of 2.5 μm thickness or bulk plastic deformation within the whole micropillar were simulated and found to reach values of 307 – 312 K in axial and 298 – 300 K in transverse direction. Even if the shear band thickness is reduced to 125 nm based on measurements performed in an earlier study [21], the maximum temperature is not rising above 315 K. The denaturation of hydrated native type 1 collagen has been reported to occur within the range of 323–343K [71–74], for mineralized collagen fibers the denaturalization temperature is reported to be 423 K [75], which is considerably higher than the maximum temperatures calculated for this study. Therefore, denaturation is not likely to occur at the strain rates imposed here. It is, however, expected that bone tissue exhibits a drop in flow stress with rising temperature similar to other materials such as polymers [38], which could at least partly explain the thickening of shear bands and moderate increase in ultimate to plateau stress ratio at higher strain rates.

4.6. Humidity

Previous studies indicated a higher yield properties in bone in dry compared to hydrated condition at several length scales [76,77,21]. This is most likely due to changes in the organic phase due to dehydration. Dry collagen is stronger, but also more brittle and cannot dissipate a lot of energy through dissipative mechanisms such as fibril sliding [78,79]. Gupta et al. [7] showed that dry bone is stiffer due to the state of the organic matrix. Unal and Akkus [84] were able to show that it is the loosely bound water around the collagen that is closely related to toughness, ductility and the post-yield mechanical properties of bone. Loosely bound water is found at the length scale of the micropillars tested in the current study. It occupies the space between the MCFs binding the organic-mineral phases through electrostatic attraction (mineral) and hydrogen bonding (collagen) [80].

In order to mimic physiological conditions, the relative humidity in the test chamber was strictly controlled and held above 90%. DVS experiments showed that the maximum change in mass due to water absorption of the ovine bone used in this study is 8.3%, at a relative humidity in the chamber of 98%. At 90% relative humidity, it absorbs 7.6% water (0.7% difference). The chosen hydration method is advantageous especially for high strain rate experimentation, due to the decreased interaction of the gaseous hydration medium with the fast-moving probe compared to liquids. It was calculated that the condition in the chamber correspond to the osmotic pressure of a NaCl solution with a concentration of 0.020 mol/l or 0.1178% NaCl solution. This difference in osmotic pressure is of no large consequence for the hydration state, as shown by Andriotis et al. [41]. They tuned the osmotic pressure by increasing the concentration of polyethylene glycol (PEG) to dehydrate collagen. However, they found that salts have limited potential to influence collagen mechanics: salt ions are small enough to enter between collagen molecules unhindered (unlike when interacting

with a semipermeable membrane), therefore they do not form osmotic pressure in MCF [41]. Fluid flow within bone occurs mostly in the Haversian canals, the lacuna-canalicular network, and to a lesser extent in the nanoscale pores [81]. Setting the relative humidity to over 90% and continuously flushing the specimen with water vapor is sufficient to prevent the nanoscale pores from drying out.

4.7. Limitations

A limitation of the study is that only a single bone of one sheep was tested, thus it is difficult to generalize the findings. However, on the extracellular matrix level the variation in mechanical properties can be well explained by variations in mineralization and mineralized collagen fibril orientation [51,52]. In addition, the comparison to other micropillar compression studies on different species (human, bovine) show that the results obtained at similar strain rate are lying within a relatively small range of 60 MPa [33,51,52]. Another limitation is the small number of FIB cross sections and TEM analyses performed. This is a result of the time consuming preparation needed for these techniques. While performing experiments on a large number of biological replicates is impossible using this technique, the advantage is that we are observing the whole tested region at nanometric resolution providing a wealth of information on the deformation mechanisms in isolated bone lamellae and the relation to the underlying fibrillar structure. Furthermore, we minimized potential bias in the obtained results by choosing micropillars based on the representativeness of their yield properties and deformation mechanisms investigated by post-test HRSEM imaging. Other limitations of this study include the presence of friction between the flat punch and the micropillar leading to tensile strains at the micropillar top surface and a localization of damage [82]. This effect is strengthened by the presence of taper in the micropillars of approximately 2.4° [83]. Furthermore, in the FIB (Tescan, Czech Republic) chamber, during the micropillar fabrication the samples are subjected to high vacuum. Submitting bone to vacuum is a non-reversible process, due to the formation of cracks that are visible on the sample's surface. However, to minimize this effect, micropillars were fabricated in regions without visible cracks. Furthermore, FIB damage, a common problem in micromechanical experiments, can be limited to a zone of less than 30 nm by stepping down with the voltage and current in consecutive milling steps [32]. Furthermore, the elastic deformation of the base, due to the micropillar sink-in, adds to the compliance of the system. However, this effect was considered in the data analysis using the Sneddon correction [43].

5. Conclusion

In this study, we compressed micropillars at the level of a single bone lamella in two orientations (46 axial and 47 transverse) with strain rates ranging from 10^{-4} s^{-1} to $8 \cdot 10^2 \text{ s}^{-1}$, and a relative humidity of over 90 % to mimic physiological conditions. In order to do so a new indenter setup was developed, capable of performing high strain rate experiments in displacement control under humid conditions. The high strain rates were specifically chosen to mimic strain rates experienced by bones during traumatic events [6].

It was found that the axially loaded bone is stronger than the transversely loaded one; however, both orientations show a clear strain rate sensitivity. Also the post-yield behavior is anisotropic; axial micropillars show strain softening, transverse ones strain hardening. The governing deformation mechanism is in both cases inelastic straining of the extrafibrillar matrix. For high strain rates, thick zones of localized shear deformation were observed.

The strain rate dependency measured here is comparable to other investigations at higher length scales as well as for different anatomical locations and species featuring different levels of mineralization. This could be an indication that the strain rate dependency is not strongly dependent on the length scale and that mineralization might not be the main driving factor for strain rate dependency. Thus, we hypothesize that the strain rate dependence is an intrinsic property of the organic phase at the nanocomposite level.

These findings shed light on the dynamic strength and deformation mechanism of bone. A better understanding of healthy bone under physiologically relevant extreme loading conditions is a missing puzzle piece that will help to better discern and quantify the changes to bone quality of patients in the presence of bone diseases using multiscale approaches. Applying the proposed methodology to human bones will help to better understand the effects of metabolic conditions such as osteoporosis on the tissue level properties and their role in the overall fracture resistance of this hierarchically organized tissue.

Declaration of Competing Interest

The authors declare that they have no known competing financial interests or personal relationships that could have appeared to influence the work reported in this paper.

Acknowledgements

CP and JS acknowledge funding through SNSF Ambizione grant no. 174192. RR acknowledges funding from the EMPAPOSTDOCS-II programme funded by the European Union's Horizon 2020 research and innovation programme under the Marie Skłodowska-Curie grant agreement number 754364. The authors would like to thank C. Hain for proof reading.

References

- [1] L.J. Melton, E.J. Atkinson, M.K. O'Connor, W.M. O'Fallon, B.L. Riggs, Bone density and fracture risk, *Med. J. Aust.* 189 (2008) 7–8, doi:10.5694/j.1326-5377.2008.tb01885.x.
- [2] T.D. Rachner, S. Khosla, L.C. Hofbauer, Osteoporosis: Now and the future, *Lancet* 377 (2011) 1276–1287, doi:10.1016/S0140-6736(10)62349-5.
- [3] J.J. Schwiedrzik, P.K. Zysset, An anisotropic elastic-viscoplastic damage model for bone tissue, *Biomech. Model. Mechanobiol.* 12 (2013) 201–213, doi:10.1007/s10237-012-0392-9.
- [4] S. Scheiner, P. Pivonka, C. Hellmich, Coupling systems biology with multiscale mechanics, for computer simulations of bone remodeling, *Comput. Methods Appl. Mech. Eng.* 254 (2013) 181–196, doi:10.1016/j.cma.2012.10.015.
- [5] S.C.E. Schuit, M. Van Der Klift, A.E.A.M. Weel, C.E.D.H. De Laet, H. Burger, E. Seeman, A. Hofman, A.G. Uitterlinden, J.P.T.M. Van Leeuwen, H.A.P. Pols, Fracture incidence and association with bone mineral density in elderly men and women: The Rotterdam Study, *Bone* 34 (2004) 195–202, doi:10.1016/j.bone.2003.10.001.
- [6] U. Hansen, P. Zioupos, R. Simpson, J.D. Currey, D. Hynd, The effect of strain rate on the mechanical properties of human cortical bone, *J. Biomech. Eng.* 130 (2008) 1–8, doi:10.1115/1.2838032.
- [7] H.S. Gupta, W. Wagermaier, G.A. Zickler, D.R. Ben Aroush, S.S. Funari, P. Roschger, H.D. Wagner, P. Fratzl, Nanoscale deformation mechanisms in bone, *Nano Lett* 5 (2005) 2108–2111, doi:10.1021/nl051584b.
- [8] H. Peterlik, P. Roschger, K. Klaushofer, P. Fratzl, From brittle to ductile fracture of bone, *Nat. Mater.* 5 (2006) 52–55, doi:10.1038/nmat1545.
- [9] J.Y. Rho, T.Y. Tsui, G.M. Pharr, Elastic properties of human cortical and trabecular lamellar bone measured by nanoindentation, *Biomaterials* 18 (1997) 1325–1330, doi:10.1016/S0142-9612(97)00073-2.
- [10] R.O. Ritchie, M.J. Buehler, P. Hansma, Built primarily from collagen molecules, mineral, (2009). www.physicstoday.org.
- [11] H. Madupalli, B. Pavan, M.M.J. Tecklenburg, Carbonate substitution in the mineral component of bone: Discriminating the structural changes, simultaneously imposed by carbonate in A and B sites of apatite, *J. Solid State Chem.* 255 (2017) 27–35, doi:10.1016/j.jssc.2017.07.025.
- [12] S. Weiner, H.D. Wagner, The material bone: Structure-mechanical function relations, *Annu. Rev. Mater. Sci.* 28 (1998) 271–298, doi:10.1146/annurev.matsci.28.1.271.
- [13] S. Schrof, P. Varga, L. Galvis, K. Raum, A. Masic, 3D Raman mapping of the collagen fibril orientation in human osteonal lamellae, *J. Struct. Biol.* 187 (2014) 266–275, doi:10.1016/j.jsb.2014.07.001.

- [14] W. Wagermaier, H.S. Gupta, A. Gourrier, M. Burghammer, P. Roschger, P. Fratzl, Spiral twisting of fiber orientation inside bone lamellae, *Biointerphases* 1 (2006) 1–5, doi:[10.1116/1.2178386](https://doi.org/10.1116/1.2178386).
- [15] P. Fratzl, R. Weinkamer, Nature's hierarchical materials, *Prog. Mater. Sci.* 52 (2007) 1263–1334, doi:[10.1016/j.pmatsci.2007.06.001](https://doi.org/10.1016/j.pmatsci.2007.06.001).
- [16] B. Yu, A. Pacureanu, C. Olivier, P. Cloetens, F. Peyrin, Assessment of the human bone lacuno-canalicular network at the nanoscale and impact of spatial resolution, *Sci. Rep.* (2020) 10, doi:[10.1038/s41598-020-61269-8](https://doi.org/10.1038/s41598-020-61269-8).
- [17] P. Schneider, M. Meier, R. Wepf, R. Müller, Towards quantitative 3D imaging of the osteocyte lacuno-canalicular network, *Bone* 47 (2010) 848–858, doi:[10.1016/j.bone.2010.07.026](https://doi.org/10.1016/j.bone.2010.07.026).
- [18] J.Y. Rho, L. Kuhn-Spearing, P. Zioupos, Mechanical properties and the hierarchical structure of bone, *Med. Eng. Phys.* 20 (1998) 92–102, doi:[10.1016/S1350-4533\(98\)00007-1](https://doi.org/10.1016/S1350-4533(98)00007-1).
- [19] T.A. Franz-Odenaal, B.K. Hall, P.E. Witten, Buried alive: How osteoblasts become osteocytes, *Dev. Dyn.* 235 (2006) 176–190, doi:[10.1002/dvdy.20603](https://doi.org/10.1002/dvdy.20603).
- [20] V. Ziv, H.D. Wagner, S. Weiner, Microstructure-microhardness relations in parallel-fibered and lamellar bone, *Bone* 18 (1996) 417–428, doi:[10.1016/8756-3282\(96\)00049-X](https://doi.org/10.1016/8756-3282(96)00049-X).
- [21] J. Schwiedrzik, A. Taylor, D. Casari, U. Wolfram, P. Zysset, J. Michler, Nanoscale deformation mechanisms and yield properties of hydrated bone extracellular matrix, *Acta Biomater* 60 (2017) 302–314, doi:[10.1016/j.actbio.2017.07.030](https://doi.org/10.1016/j.actbio.2017.07.030).
- [22] X.J. Wang, Y.C. Li, P.D. Hodgson, C.E. Wen, Nano-and macro-scale characterization of the mechanical properties of bovine bone, *Mater. Forum.* 31 (2007) 156–159.
- [23] V. Ebacher, C. Tang, H. McKay, T.R. Oxland, P. Guy, R. Wang, Strain redistribution and cracking behavior of human bone during bending, *Bone* 40 (2007) 1265–1275, doi:[10.1016/j.bone.2006.12.065](https://doi.org/10.1016/j.bone.2006.12.065).
- [24] A. Sharir, M.M. Barak, R. Shahar, Whole bone mechanics and mechanical testing, *Vet. J.* 177 (2008) 8–17, doi:[10.1016/j.tvjl.2007.09.012](https://doi.org/10.1016/j.tvjl.2007.09.012).
- [25] H.B. Hunt, E. Donnelly, Bone Quality Assessment Techniques: Geometric, Compositional, and Mechanical Characterization from Macroscale to Nanoscale, *Clin. Rev. Bone Miner. Metab.* 14 (2016) 133–149, doi:[10.1007/s12018-016-9222-4](https://doi.org/10.1007/s12018-016-9222-4).
- [26] H.S. Gupta, P. Fratzl, M. Kerschnitzki, G. Benecke, W. Wagermaier, H.O.K. Kirchner, Evidence for an elementary process in bone plasticity with an activation enthalpy of 1 eV, *J. R. Soc. Interface.* 4 (2007) 277–282, doi:[10.1098/rsif.2006.0172](https://doi.org/10.1098/rsif.2006.0172).
- [27] Z. Fan, J.Y. Rho, Effects of viscoelasticity and time-dependent plasticity on nanoindentation measurements of human cortical bone, *J. Biomed. Mater. Res.* – Part A. 67 (2003) 208–214, doi:[10.1002/jbm.a.10027](https://doi.org/10.1002/jbm.a.10027).
- [28] H. Isaksson, S. Nagao, M. Makiwicz, P. Julkunen, R. Nowak, J.S. Jurvelin, Precision of nanoindentation protocols for measurement of viscoelasticity in cortical and trabecular bone, *J. Biomech.* 43 (2010) 2410–2417, doi:[10.1016/j.jbiomech.2010.04.017](https://doi.org/10.1016/j.jbiomech.2010.04.017).
- [29] P.K. Zysset, X. Edward Guo, C. Edward Hoffer, K.E. Moore, S.A. Goldstein, Elastic modulus and hardness of cortical and trabecular bone lamellae measured by nanoindentation in the human femur, *J. Biomech.* 32 (1999) 1005–1012, doi:[10.1016/S0021-9290\(99\)00111-6](https://doi.org/10.1016/S0021-9290(99)00111-6).
- [30] K.W. Luczynski, A. Steiger-Thirfield, J. Bernardi, J. Eberhardsteiner, C. Hellmich, Extracellular bone matrix exhibits hardening elastoplasticity and more than double cortical strength: Evidence from homogeneous compression of non-tapered single micron-sized pillars welded to a rigid substrate, *J. Mech. Behav. Biomed. Mater.* 52 (2015) 51–62, doi:[10.1016/j.jmbbm.2015.03.001](https://doi.org/10.1016/j.jmbbm.2015.03.001).
- [31] A. Groetsch, A. Gourrier, J. Schwiedrzik, M. Sztucki, R.J. Beck, J.D. Shephard, J. Michler, P.K. Zysset, U. Wolfram, Compressive behaviour of uniaxially aligned individual mineralised collagen fibres at the micro- and nanoscale, *Acta Biomater* 89 (2019) 313–329, doi:[10.1016/j.actbio.2019.02.053](https://doi.org/10.1016/j.actbio.2019.02.053).
- [32] J. Schwiedrzik, R. Raghavan, A. Bürki, V. Lenader, U. Wolfram, J. Michler, P. Zysset, In situ micropillar compression reveals superior strength and ductility but an absence of damage in lamellar bone, *Nat. Mater.* 13 (2014) 740–747, doi:[10.1038/nmat3959](https://doi.org/10.1038/nmat3959).
- [33] O.A. Tertuliano, J.R. Greer, The nanocomposite nature of bone drives its strength and damage resistance, *Nat. Mater.* 15 (2016) 1195–1202, doi:[10.1038/nmat4719](https://doi.org/10.1038/nmat4719).
- [34] M.D. Uchic, D.M. Dimiduk, J.N. Florando, W.D. Nix, Sample dimensions influence strength and crystal plasticity, *Science* 305 (80) (2004) 986–989, doi:[10.1126/science.1098993](https://doi.org/10.1126/science.1098993).
- [35] J.P. Best, G. Guillonnet, S. Grop, A.A. Taylor, D. Frey, Q. Longchamp, T. Schär, M. Morstein, J.M. Breguet, J. Michler, High temperature impact testing of a thin hard coating using a novel high-frequency in situ micromechanical device, *Surf. Coatings Technol.* 333 (2018) 178–186, doi:[10.1016/j.surfcoat.2017.10.072](https://doi.org/10.1016/j.surfcoat.2017.10.072).
- [36] G. Guillonnet, M. Miesza, J. Wehrs, J. Schwiedrzik, S. Grop, D. Frey, L. Philippe, J.M. Breguet, J. Michler, J.M. Wheeler, Nanomechanical testing at high strain rates: New instrumentation for nanoindentation and microcompression, *Mater. Des.* 148 (2018) 39–48, doi:[10.1016/j.matdes.2018.03.050](https://doi.org/10.1016/j.matdes.2018.03.050).
- [37] R. Ramachandramoorthy, J. Schwiedrzik, L. Petho, C. Guerra-Nunez, D. Frey, J.M. Breguet, J. Michler, Dynamic Plasticity and Failure of Microscale Glass: Rate-Dependent Ductile-Brittle-Ductile Transition, *Nano Lett* 19 (2019) 2350–2359, doi:[10.1021/acs.nanolett.8b05024](https://doi.org/10.1021/acs.nanolett.8b05024).
- [38] N. Rohbeck, R. Ramachandramoorthy, D. Casari, P. Schürch, T.E.J. Edwards, L. Schilinsky, L. Philippe, J. Schwiedrzik, J. Michler, Effect of high strain rates and temperature on the micromechanical properties of 3D-printed polymer structures made by two-photon lithography, *Mater. Des.* 195 (2020) 1–9, doi:[10.1016/j.matdes.2020.108977](https://doi.org/10.1016/j.matdes.2020.108977).
- [39] M.L. Moritz, Why 0.9% saline is isotonic: understanding the aqueous phase of plasma and the difference between osmolality and osmolarity, *Pediatr. Nephrol.* 34 (2019) 1299–1300, doi:[10.1007/s00467-018-4084-2](https://doi.org/10.1007/s00467-018-4084-2).
- [40] H. Li, S. ren Sun, J.Q. Yap, J. hua Chen, Q. Qian, 0.9% Saline Is Neither Normal Nor Physiological, *J. Zhejiang Univ. Sci. B.* 17 (2016) 181–187, doi:[10.1631/jzus.B1500201](https://doi.org/10.1631/jzus.B1500201).
- [41] O.G. Andriotis, S. Desissaire, P.J. Thurner, Collagen Fibrils: Nature's Highly Tunable Nonlinear Springs, *ACS Nano* 12 (2018) 3671–3680, doi:[10.1021/acsnano.8b00837](https://doi.org/10.1021/acsnano.8b00837).
- [42] P. Grönquist, M. Frey, T. Keplinger, I. Burgert, Mesoporosity of Delignified Wood Investigated by Water Vapor Sorption, *ACS Omega* 4 (2019) 12425–12431, doi:[10.1021/acsomega.9b00862](https://doi.org/10.1021/acsomega.9b00862).
- [43] H. Zhang, B.E. Schuster, Q. Wei, K.T. Ramesh, The design of accurate micro-compression experiments, *Scr. Mater.* 54 (2006) 181–186, doi:[10.1016/j.scriptamat.2005.06.043](https://doi.org/10.1016/j.scriptamat.2005.06.043).
- [44] D.R. Carter, W.C. Hayes, Bone Compressive Strength, *Science* 194 (80) (1976) 1174–1176.
- [45] J. Wehrs, G. Mohanty, G. Guillonnet, A.A. Taylor, X. Maeder, D. Frey, L. Philippe, S. Mischler, J.M. Wheeler, J. Michler, Comparison of In Situ Micromechanical Strain-Rate Sensitivity Measurement Techniques, *Jom* 67 (2015) 1684–1693, doi:[10.1007/s11837-015-1447-z](https://doi.org/10.1007/s11837-015-1447-z).
- [46] D. Caillard, J.L. Martin, Thermally activated mechanisms in crystal plasticity, Pergamon, Burlington, 2003. <http://books.google.com/books?hl=en&lr=&id=VPblvN7SkkC&oi=fnd&pg=PP1&dq=Thermally+activated+mechanisms+in+crystal+plasticity&ots=iJShXLiHnx&sig=Ekl0SD2oeA-MaGsm2eihBKNbXFM>.
- [47] T.E. Brady, G.S.Y. Yeh, Mechanism of Yielding and Cold Flow in Glassy Polymers, *J. Macromol. Sci. Part B.* 9 (1974) 659–697, doi:[10.1080/0022347408204557](https://doi.org/10.1080/0022347408204557).
- [48] J.M. Wheeler, L. Thilly, A. Morel, A.A. Taylor, A. Montagne, R. Ghisleni, J. Michler, The plasticity of indium antimonide: Insights from variable temperature, strain rate jump micro-compression testing, *Acta Mater* 106 (2016) 283–289, doi:[10.1016/j.actamat.2015.12.036](https://doi.org/10.1016/j.actamat.2015.12.036).
- [49] A. Feldmann, P. Wili, G. Maquer, P. Zysset, The thermal conductivity of cortical and cancellous bone, *Eur. Cells Mater.* 35 (2018) 25–33, doi:[10.22203/ecm.v035a03](https://doi.org/10.22203/ecm.v035a03).
- [50] E.A. McNally, H.P. Schwarcz, G.A. Botton, A.L. Arsenault, A model for the ultrastructure of bone based on electron microscopy of ion-milled sections, *PLoS One* 7 (2012) 1–12, doi:[10.1371/journal.pone.0029258](https://doi.org/10.1371/journal.pone.0029258).
- [51] T. Kochetkova, C. Peruzzi, O. Braun, J. Overbeck, A.K. Maurya, A. Neels, M. Calame, J. Michler, P. Zysset, J. Schwiedrzik, Combining polarized Raman spectroscopy and micropillar compression to study microscale structure-property relationships in mineralized tissues, *Acta Biomater* 119 (2021) 390–404, doi:[10.1016/j.actbio.2020.10.034](https://doi.org/10.1016/j.actbio.2020.10.034).
- [52] M. Indermaur, D. Casari, T. Kochetkova, C. Peruzzi, E. Zimmermann, F. Rauch, B. Willie, J. Michler, J. Schwiedrzik, P. Zysset, Compressive Strength of Iliac Bone ECM Is Not Reduced in Osteogenesis Imperfecta and Increases With Mineralization, *J. Bone Miner. Res.* (2021) 1–12 00, doi:[10.1002/jbmr.4286](https://doi.org/10.1002/jbmr.4286).
- [53] A.G. Reisinger, D.H. Pahr, P.K. Zysset, Principal stiffness orientation and degree of anisotropy of human osteons based on nanoindentation in three distinct planes, *J. Mech. Behav. Biomed. Mater.* 4 (2011) 2113–2127, doi:[10.1016/j.jmbbm.2011.07.010](https://doi.org/10.1016/j.jmbbm.2011.07.010).
- [54] D.T. Reilly, A.H. Burstein, The elastic and ultimate properties of compact bone tissue, *J. Biomech.* 8 (1975), doi:[10.1016/0021-9290\(75\)90075-5](https://doi.org/10.1016/0021-9290(75)90075-5).
- [55] R.M. Kulini, P.Y. Chen, F. Jiang, K.S. Vecchio, A study of the dynamic compressive behavior of Elk antler, *Mater. Sci. Eng. C.* 31 (2011) 1030–1041, doi:[10.1016/j.msec.2011.03.002](https://doi.org/10.1016/j.msec.2011.03.002).
- [56] S. Pang, Y. Liang, W. Tao, Y. Liu, S. Huan, H. Qin, Effect of the strain rate and fiber direction on the dynamic mechanical properties of beechwood, *Forests* 10 (2019). <https://doi.org/10.3390/f10100881>.
- [57] K. Tai, F.J. Ulm, C. Ortiz, Nanogranular origins of the strength of bone, *Nano Lett* 6 (2006) 2520–2525, doi:[10.1021/nl061877k](https://doi.org/10.1021/nl061877k).
- [58] P. De Falco, E. Barbieri, N. Pugno, H.S. Gupta, Staggered Fibrils and Damageable Interfaces Lead Concurrently and Independently to Hysteretic Energy Absorption and Inhomogeneous Strain Fields in Cyclically Loaded Antler Bone, *ACS Biomater. Sci. Eng.* 3 (2017) 2779–2787, doi:[10.1021/acsbomaterials.6b00637](https://doi.org/10.1021/acsbomaterials.6b00637).
- [59] T.P.M. Johnson, S. Socrate, M.C. Boyce, A viscoelastic, viscoplastic model of cortical bone valid at low and high strain rates, *Acta Biomater* 6 (2010) 4073–4080, doi:[10.1016/j.actbio.2010.04.017](https://doi.org/10.1016/j.actbio.2010.04.017).
- [60] D. Casari, J. Michler, P. Zysset, J. Schwiedrzik, Microtensile properties and failure mechanisms of cortical bone at the lamellar level, *Acta Biomater* 120 (2021) 135–145, doi:[10.1016/j.actbio.2020.04.030](https://doi.org/10.1016/j.actbio.2020.04.030).
- [61] M.L. Oyen, T.A.V. Shean, D.G.T. Strange, M. Gallii, Size effects in indentation of hydrated biological tissues, *J. Mater. Res.* 27 (2012) 245–255, doi:[10.1557/jmr.2011.322](https://doi.org/10.1557/jmr.2011.322).
- [62] P.M. Buechner, R.S. Lakes, Size effects in the elasticity and viscoelasticity of bone, *Biomech. Model. Mechanobiol.* 1 (2003) 295–301, doi:[10.1007/s10237-002-0026-8](https://doi.org/10.1007/s10237-002-0026-8).
- [63] M.A.K. Liebschner, T.S. Keller, Hydraulic strengthening affects the stiffness and strength of cortical bone, *Ann. Biomed. Eng.* 33 (2005) 26–38, doi:[10.1007/s10439-005-8960-0](https://doi.org/10.1007/s10439-005-8960-0).
- [64] J. Richeton, S. Azhi, K.S. Vecchio, F.C. Jiang, R.R. Adharapurapu, Influence of temperature and strain rate on the mechanical behavior of three amorphous polymers: Characterization and modeling of the compressive yield stress, *Int. J. Solids Struct.* 43 (2006) 2318–2335, doi:[10.1016/j.jislsolstr.2005.06.040](https://doi.org/10.1016/j.jislsolstr.2005.06.040).

- [65] S. Pimenta, R. Gutkin, S.T. Pinho, P. Robinson, A micromechanical model for kink-band formation: Part I - Experimental study and numerical modelling, *Compos. Sci. Technol.* 69 (2009) 948–955, doi:[10.1016/j.compscitech.2009.02.010](https://doi.org/10.1016/j.compscitech.2009.02.010).
- [66] G. Markeset, H. Arne, (Communicated by Z.P. Bazant) (Received March 7.1995), *Science* (80-.). 25 (1995) 702–708.
- [67] X. Chen, Y. Li, Z. Zhi, Y. Guo, N. Ouyang, The compressive and tensile behavior of a 0/90 C fiber woven composite at high strain rates, *Carbon N. Y.* 61 (2013) 97–104, doi:[10.1016/j.carbon.2013.04.073](https://doi.org/10.1016/j.carbon.2013.04.073).
- [68] M. Wendlandt, T.A. Tervoort, U.W. Suter, Non-linear, rate-dependent strain-hardening behavior of polymer glasses, *Polymer (Guildf)* 46 (2005) 11786–11797, doi:[10.1016/j.polymer.2005.08.079](https://doi.org/10.1016/j.polymer.2005.08.079).
- [69] M. Wendlandt, T.A. Tervoort, U.W. Suter, Strain-hardening modulus of cross-linked glassy poly(methyl methacrylate), *J. Polym. Sci. Part B Polym. Phys.* 48 (2010) 1464–1472, doi:[10.1002/polb.21979](https://doi.org/10.1002/polb.21979).
- [70] M.O. Robbins, R.S. Hoy, Scaling of the strain hardening modulus of glassy polymers with the flow stress, *J. Polym. Sci. Part B Polym. Phys.* 47 (2009) 1406–1411, doi:[10.1002/polb.21734](https://doi.org/10.1002/polb.21734).
- [71] L. Bozec, M. Odlyha, Thermal denaturation studies of collagen by microthermal analysis and atomic force microscopy, *Biophys. J.* 101 (2011) 228–236, doi:[10.1016/j.bpj.2011.04.033](https://doi.org/10.1016/j.bpj.2011.04.033).
- [72] S. McPhee, A. Groetsch, J.D. Shephard, U. Wolfram, Heat impact during laser ablation extraction of mineralised tissue micropillars, *Sci. Rep.* 11 (2021) 1–13, doi:[10.1038/s41598-021-89181-9](https://doi.org/10.1038/s41598-021-89181-9).
- [73] Y. Sun, W.L. Chen, S.J. Lin, S.H. Jee, Y.F. Chen, L.C. Lin, P.T.C. So, C.Y. Dong, Investigating mechanisms of collagen thermal denaturation by high resolution second-harmonic generation imaging, *Biophys. J.* 91 (2006) 2620–2625, doi:[10.1529/biophysj.106.085902](https://doi.org/10.1529/biophysj.106.085902).
- [74] H. Trębacz, A. Szczesna, M. Arczewska, Thermal stability of collagen in naturally ageing and in vitro glycosylated rabbit tissues, *J. Therm. Anal. Calorim.* 134 (2018) 1903–1911, doi:[10.1007/s10973-018-7375-8](https://doi.org/10.1007/s10973-018-7375-8).
- [76] X. Wang, R.A. Bank, J.M. TeKoppele, C. Mauli Agrawal, The role of collagen in determining bone mechanical properties, *J. Orthop. Res.* 19 (2001) 1021–1026, doi:[10.1016/S0736-0266\(01\)00047-X](https://doi.org/10.1016/S0736-0266(01)00047-X).
- [76] N. Rodriguez-Florez, M.L. Oyen, S.J. Shefelbine, Insight into differences in nanoindentation properties of bone, *J. Mech. Behav. Biomed. Mater.* 18 (2013) 90–99, doi:[10.1016/j.jmbbm.2012.11.005](https://doi.org/10.1016/j.jmbbm.2012.11.005).
- [77] J.S. Nyman, A. Roy, X. Shen, R.L. Acuna, J.H. Tyler, X. Wang, The influence of water removal on the strength and toughness of cortical bone, *J. Biomech.* 39 (2006) 931–938, doi:[10.1016/j.jbiomech.2005.01.012](https://doi.org/10.1016/j.jbiomech.2005.01.012).
- [78] M.J. Buehler, Nature designs tough collagen: Explaining the nanostructure of collagen fibrils, *Proc. Natl. Acad. Sci. U. S. A.* 103 (2006) 12285–12290, doi:[10.1073/pnas.0603216103](https://doi.org/10.1073/pnas.0603216103).
- [79] G.E. Fantner, T. Hassenkam, J.H. Kindt, J.C. Weaver, H. Birkedal, L. Pechenik, J.A. Cutroni, G.A.G. Cidade, G.D. Stucky, D.E. Morse, P.K. Hansma, Sacrificial bonds and hidden length dissipate energy as mineralized fibrils separate during bone fracture, *Nat. Mater.* 4 (2005) 612–616, doi:[10.1038/nmat1428](https://doi.org/10.1038/nmat1428).
- [80] M. Unal, A. Creecy, J.S. Nyman, The Role of Matrix Composition in the Mechanical Behavior of Bone, *Curr. Osteoporos. Rep.* 16 (2018) 205–215, doi:[10.1007/s11914-018-0433-0](https://doi.org/10.1007/s11914-018-0433-0).
- [81] M.L. Knothe Tate, Whither flows the fluid in bone?" An osteocyte's perspective, *J. Biomech.* 36 (2003) 1409–1424, doi:[10.1016/S0021-9290\(03\)00123-4](https://doi.org/10.1016/S0021-9290(03)00123-4).
- [82] P.R. Howie, S. Korte, W.J. Clegg, Fracture modes in micropillar compression of brittle crystals, *J. Mater. Res.* 27 (2012) 141–151, doi:[10.1557/jmr.2011.256](https://doi.org/10.1557/jmr.2011.256).
- [83] R. Lacroix, G. Kermouche, J. Teisseire, E. Barthel, Plastic deformation and residual stresses in amorphous silica pillars under uniaxial loading, *Acta Mater* 60 (2012) 5555–5566, doi:[10.1016/j.actamat.2012.07.016](https://doi.org/10.1016/j.actamat.2012.07.016).
- [84] M. Unal, O. Akkus, Raman spectral classification of mineral- and collagen-bound water's associations to elastic and post-yield mechanical properties of cortical bone, *Bone* 81 (2015) 315–326 <http://dx.doi.org/10.1016/j.bone.2015.07.024>, doi:[10.1016/j.bone.2015.07.024](https://doi.org/10.1016/j.bone.2015.07.024).